Frequency super-resolution with spectro-temporal shaping of photons

Manav Shah and Linran Fan*
James C. Wyant College of Optical Sciences, 1630 E. University Blvd., Tucson, AZ - 85721
(Dated: June 14, 2021)

Quantum sensing and metrology promise new insights and novel techniques to surpass the measurement limits of classical framework. Significant improvement has been made in the areas of imaging, positioning, timing, interferometry, communication and information processing through quantum detection and estimation techniques. In this Letter, we focus on the application of quantum information for spectral measurements. Specifically, we study the quantum limit to resolve two spectral modes with small frequency separation. We show that frequency super-resolution can be achieved with spectro-temporal shaping of input fields before detection. Through a numerical optimization algorithm, we design the apparatus for spectro-temporal shaping based on phase modulation and dispersion engineering. This scheme can achieve performance close to the quantum limit with minimum resources, showing the robustness for experimental implementation and real-world applications.

I. INTRODUCTION

Improving the accuracy and precision of spectral measurements is a topic of both scientific and technological importance. Increasingly sophisticated spectroscopy is utilized in wide applications such as metrology [1–5], optical atomic clocks [6–9], chemical and biological analysis [10–12], and ultrafast processes [13, 14]. Techniques like frequency chain [15, 16], optical frequency combs from mode-locked pulse lasers [17–19], electro-optic modulation [20, 21], optical microcombs [22–24], as well as spectro-temporal magnifiers [25–28] have been developed to this end.

In spite of the impressive progress in newly developed techniques, the standard configuration for spectrometers and optical spectrum analyzers consists of a dispersive element followed by direct detection. The equivalence between paraxial imaging and narrowband dispersion [29] indicates that direct spectral measurement suffers from Rayleigh's limit akin to spatial imaging [30] - the error in resolving two frequency modes grows infinitely large as their separation approaches zero. The resolution of standard spectral measurements is thus limited by the performance of dispersive elements.

A recent study based on quantum estimation theory showed that resolution beyond spatial Rayleigh limit can be achieved with linear optics and photon counting regardless of fluorescence control [31]. This is due to the significant gap between the error produced by direct imaging and the fundamental quantum error limit that can be achieved asymptotically [32]. This approach has been further explored theoretically and experimentally [33–35] for super-resolution imaging. In contrast to this, approaches to realize frequency super-resolution have been rarely explored [36, 37].

In this paper, we propose to use spectro-temporal shaping of photons to overcome the resolution limit for frequency measurement. The quantum limit to resolve two incoherent spectral modes with small frequency separation is explored. Instead of using simple dispersive elements, we implement spectro-temporal shaping of photons with multiple stages of phase modulation and dispersion engineering before detection. By only detecting the mode carrying the maximum information about frequency separation, we can achieve frequency resolution significantly higher than Rayleigh limit. We further develop two complementary approaches for spectro-temporal shaping, based on dispersion optimization and arbitrary-wave modulation respectively. Both approaches can achieve quantum advantages robustly, providing high flexibility for future experimental demonstrations and practical implementations. We further examine the effects of noise and measurement errors on our approach and discuss the minimum resource re-

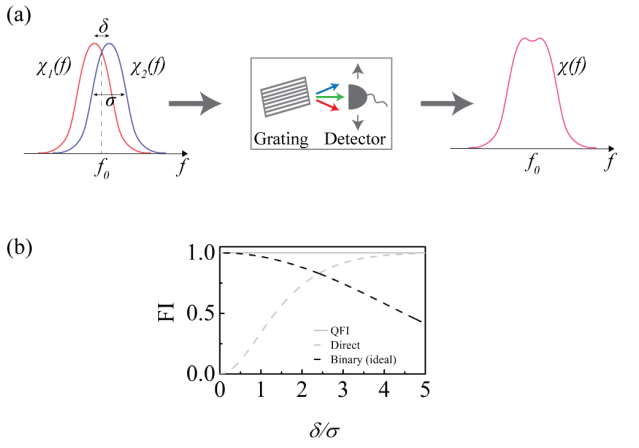

FIG. 1. (a) Schematic of standard frequency measurement approach: two frequency modes with small separation go through dispersive elements followed by direct detection; (b) Fisher information for different approaches to measure frequency separation. Solid grey: Quantum Fisher information; Dashed grey: dispersive elements with direct detection; Dashed black: binary HG mode detection.

* lfan@optics.arizona.edu

quirement to achieve quantum advantages.

II. CLASSICAL AND QUANTUM LIMITS

Frequency resolution for spectral imaging depends on the ability to precisely estimate the separation between two frequency modes. The optimal measurement results in minimal possible error in estimating frequency separation allowed by the Cramer-Rao inequality [38, 39].

Consider a state ρ that depends on a single, unknown parameter x. We can devise an unbiased estimator for x by performing a measurement on ρ. If y is the measurement output, classical Fisher Information (FI) for estimating x is calculated as [40]

$$J(x) = \int dy \frac{\partial^2}{\partial x^2}\Big(\log[p(y|x)]\Big). \tag{1}$$

The resultant root-mean-squared error (denoted by Δx) from measurement over n copies of ρ is limited by the *classical* Cramer-Rao bound [38, 39]

$$\Delta x \geq \frac{1}{\sqrt{nJ(x)}} \tag{2}$$

which is conditioned on the classical probability $p(y|x) = Tr[\rho(x)\Pi(y)]$ induced by a specific measurement $\Pi(y)$. The fundamental quantum mechanical bound for error Δx is obtained by considering all possible measurements that may be performed on quantum state $\rho(x)$. This *quantum* Cramer-Rao bound (QCRB) is given by [41]

$$\Delta x \geq \frac{1}{\sqrt{nJ(x)}} \geq \frac{1}{\sqrt{nK(x)}} \tag{3}$$

where K is the quantum Fisher information (QFI). In contrast to its classical counterpart, the QFI is not specific to any particular measurement and depends only on the initial state $\rho(x)$,

$$K(x) = Re\Big[Tr\big[\mathcal{L}^2\rho(x)\big]\Big] \tag{4}$$

where $\mathcal{L}$ is the symmetric-logarithmic derivative operator acting on ρ [42].

The measurement that achieves this minimum possible error ($\Delta x = (nK(x))^{-1/2}$) yields FI ($J$) that is equal to QFI ($K$). While QCRB provides the minimum achievable error Δx, it does not specify the measurement (or estimator) that can achieve it [32].

We now direct our focus to the determination of frequency resolution for spectral measurements. This resolution limit is determined by the minimum possible frequency separation that can be estimated precisely between overlapping spectral modes. Figure 1a shows the schematic of direct detection of two mutually incoherent Gaussian spectra ($\chi_1(f)$ and $\chi_2(f)$) with constant bandwidth σ and separation δ. We assume to have prior knowledge of the center frequency f_0 and set it to zero without loss of generality. We use a Gaussian mode profile here for simplicity, although a similar approach may be applied for arbitrary input modes [43].

The input spectrum ($\chi(f)$) can be written with single unknown parameter (relative frequency separation δ),

$$\chi(f) = \frac{1}{\sqrt{2\pi\sigma^2}}\Big(e^{-\frac{(f-\delta)^2}{2\sigma^2}} + e^{-\frac{(f+\delta)^2}{2\sigma^2}}\Big). \tag{5}$$

Using direct detection to estimate δ, a photon count is registered at frequency f with probability $p(f|\delta) = \chi(f)$. As δ is decreased, the overlap between the modes increases and it becomes difficult to estimate δ precisely due to an arbitrarily high estimation error ($\Delta\delta$). However, this limitation is imposed by direct detection, and can be surpassed by the proper design of a different measurement approach.

It has been shown that QFI is independent of source separation for spatial imaging and pre-detection spatial Hermite-Gaussian (HG) mode decomposition achieves this limit [31]. Due to the equivalence between paraxial imaging and narrowband dispersion, it is straightforward to show that QFI for frequency estimation also remains constant while frequency separation δ decreases [37]. For the case of Gaussian spectral modes,

$$K(\delta) \equiv K = \frac{N}{4\sigma^2} \tag{6}$$

where N is the average photon number detected. Figure 1b shows that FI for direct spectral imaging (from Eq. 1) approaches QFI limit (constant, K) for large frequency separation δ. However, as δ approaches zero, it drops rapidly to zero, and the frequency resolution is bounded by an equivalent Rayleigh limit.

We decompose the spectrum $\chi(f)$ into spectral HG modes [44] before detection to saturate the QFI limit. The probability of detecting a photon in mode m is given by $P_m = \frac{1}{2}(|\langle v_m|\chi_1\rangle|^2 + |\langle v_m|\chi_2\rangle|^2)$, where v_m represents the m^{th} HG mode. The resultant FI can be calculated from Eq. 1 as,

$$J_{full}(\delta) = \sum_{m=0}^{\infty} \frac{1}{P_m}\left(\frac{\partial P_m}{\partial \delta}\right)^2 \approx \frac{N}{4\sigma^2}. \tag{7}$$

Equation 7 requires spectral decomposition into an infinite number of modes to saturate the QFI limit. We can simplify the detection strategy by only detecting HG modes with maximum information about frequency separation. In the small-δ regime, the HG_1 mode contains nearly all information about separation δ while HG_0 mode does not contribute to FI [45]. Also, decomposition amplitudes for higher order ($m \geq 2$) HG modes are negligible. Therefore, a binary detection strategy can be used where HG_0 and higher order modes (cumulatively referred to as HG_1 mode) are detected separately with

probabilities

$$P_0 = e^{-\frac{\delta^2}{16\sigma^2}}, \tag{8}$$

$$P_1 = (1 - P_0) = 1 - e^{-\frac{\delta^2}{16\sigma^2}}. \tag{9}$$

The corresponding FI can be expressed as,

$$J_b(\delta) = \frac{N}{4\sigma^2}\Big(\frac{\delta^2}{16\sigma^2}\Big)\left(\frac{e^{-\frac{\delta^2}{8\sigma^2}}}{1 - e^{-\frac{\delta^2}{16\sigma^2}}}\right), \tag{10}$$

which saturates the QFI in our target parameter regime of small separation, $\delta \ll \sigma$ (Fig. 1b). At the same time, it achieves quantum advantage over direct detection for $\delta < 2\sigma$, in the region where $\chi_1(f)$ and $\chi_2(f)$ have significant overlap.

III. IMPLEMENTATION OF SPECTRO-TEMPORAL SHAPING

In order to break the classical frequency resolution limit, we explore the implementation of the binary detection scheme described in the previous section using spectro-temporal shaping of photons before detection. To realize this transformation, we use alternating spectral phase masks and temporal phase modulation (Fig. 2a) [46, 47]. The Fourier equivalence of time and frequency, along with well-established technology to control both temporal and spectral degrees of freedom, enables us to engineer spectro-temporal shaping with two complementary approaches - we fix either the temporal modulation or spectral phase masks while optimizing the other. This is in contrast to implementing spatial unitary transformations, where the approach is restricted to optimized spatial phase masks spaced by free-space propagation with little flexibility [48].

We use wavefront matching algorithm [49–51] to numerically optimize spectral phase masks or temporal modulation (in the respective approach). Numerical optimization has the advantage of realizing target transformation with high precision and small resource requirement. Although small imperfections in the numerically optimized transformation lead to increased error in δ-estimation, we show that optimized binary transformation can obtain quantum advantage in frequency resolution robustly and achieve performance close to the quantum limit. We quantify the improvement over direct detection by defining the resolution limit ($\delta_{\frac{1}{2}}$) as the frequency separation at which the particular measurement achieves FI that is half of the QFI limit. For direct detection, this definition leads to Rayleigh-like resolution limit of $\delta^{\text{direct}}_{\frac{1}{2}} = 1.34\sigma$.

A. Approach I - Optimizing spectral phase masks with fixed sinusoidal modulation

In the first approach, we use multiple stages of optimized spectral phase masks implemented with pulse shapers and fixed sinusoidal modulation (Fig. 2a). The goal is to optimize the spectral phase mask at each stage to transform the HG_0 and HG_1 modes from the input spectrum into two well-separated Gaussian modes (Fig. 2b). All phase masks are initialized as identity. The input spectrum and target output are propagated in the forward and backward directions respectively. For each HG mode (m), the overlap between the forward ($v^f_{m,l}$) and backward ($v^b_{m,l}$) propagating fields is calculated at each stage (l). The field overlap is summed over all HG modes, and its phase added to the existing phase mask. For the i^{th} optimization iteration, the updated phase phase at l^{th} stage is

$$\phi_{i,l} = \phi_{i-1,l} + \angle\Big[\sum_m (v^f_{m,l})^\dagger v^b_{m,l}\Big]. \tag{11}$$

The optimization result (phase masks and intermediate spectrum distribution) for input field with frequency separation $\delta = \sigma$ is shown in Fig. 2b. Four stages of alternating phase masks and temporal modulation are used, and the temporal modulation is sinusoidal with 2.5π modulation depth.

The field transformation shows that the numerically optimized transformation is an excellent approximation to the target mode transformation. However, any such optimization has inherent imperfections due to restricted resources, such as the number of stages. As a result, a small fraction of power for input HG modes is transformed into the wrong target output mode (modal cross-talk) that leads to noticeable deviation in FI compared to an ideal transformation [45, 52]. As δ approaches zero, the power of HG_0 mode at the input field increases, while the power of HG_1 mode decreases. Even a minute amount of cross-talk creates high uncertainty in determining the power in the HG_1 mode, which holds nearly all information about δ. This inevitable imperfection in the transformation due to restrained resources leads to the rapid decrease of FI as δ approaches zero. In spite of this deviation from the ideal case, we find that separation of HG_0 mode before detection clearly leads to higher resolution of $\delta^b_{\frac{1}{2}} = 0.83\sigma$ using only 3 stages (Fig. 3a) showing the robustness of the numerical approach. Increasingly accurate mode transformation with lower cross-talk can be achieved using more transformation stages. We obtain higher FI and better frequency resolution of $\delta^b_{\frac{1}{2}} = 0.05\sigma$ using 6 stages (Fig. 3a). This presents an improvement in resolution over direct detection by factor of ~ 27.

Another critical constraint during experimental implementation of this transformation is the frequency resolution of dispersion phase masks, limited practically by resolution of pulse shapers. Figure 3b shows the results for different frequency resolutions of phase masks using 6

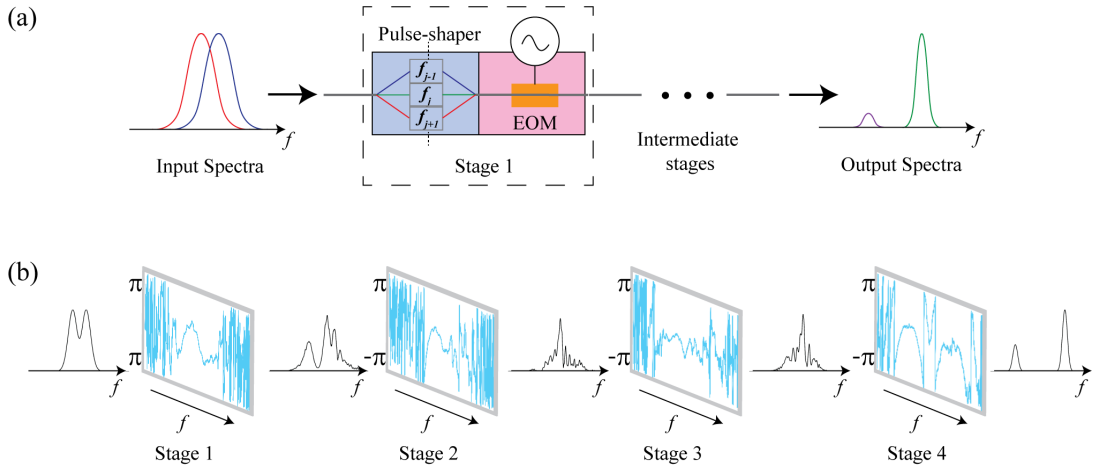

FIG. 2. (a) Schematic of spectro-temporal shaping with optimized spectral phase masks and fixed sinusoidal modulation. The fundamental and orthogonal higher-order HG modes of the input field are transformed into two well-separated Gaussian modes respectively. (b) Example results for a 4-stage spectro-temporal shaping, showing the applied spectral phase masks (black) and output spectrum distribution (black) at each stage. The modulation depth for all stages is 2.5π. The frequency separation between input spectral modes is $\delta = \sigma$. The fixed temporal modulation at each stage is hidden for convenience.

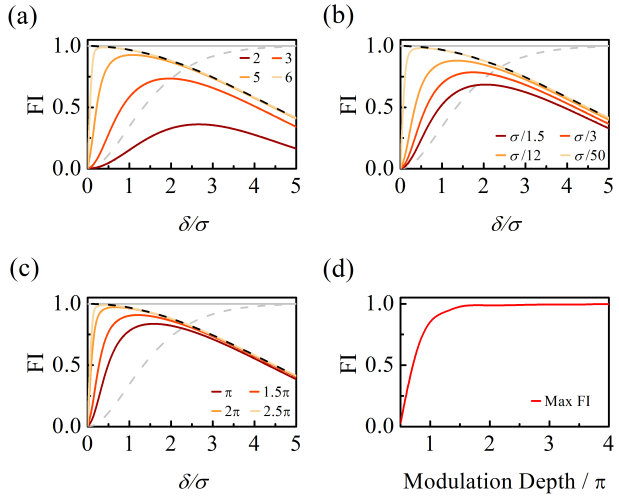

FIG. 3. Fisher information versus frequency separation optimized with (a) different numbers of transformation stages; (b) different frequency resolutions of phase masks; and (c) modulation depths. Quantum Fisher information (solid grey), Fisher information of direct detection (dashed grey), and ideal binary detection (dashed black) are also shown in (a-c). (d) Maximum achievable Fisher information with different modulation depths. Except specified, modulation depth is 2.5π, frequency resolution for phase masks is infinite, and number of transformation stages is 6.

transformation stages and a depth of 2.5π for fixed sinusoidal modulation. Decreasing the resolution of spectral phases leads to greater inaccuracy in implementing the optimized phase masks and higher cross-talk. However, even with relatively low phase resolution ($\sigma/1.5$), we can achieve frequency super-resolution with $\delta^b_{\frac{1}{2}} = 0.95\sigma$.

The modulation depth is another factor that plays a critical role in determining the accuracy of spectro-temporal shaping. Larger modulation depth ensures that a wider band of frequencies undergo mixing in a single stage, improving the efficiency of spectral transformation with fixed number of stages (Fig. 3c). A modulation depth of π enables super-resolution with $\delta^b_{\frac{1}{2}} = 0.5\sigma$. Figure 3d shows that modulation depth greater than (1.5π) is sufficient to achieve FI close to unity, indicating a near-ideal transformation.

B. Approach II - Optimizing temporal modulation with constant group velocity dispersion

Instead of optimizing spectral phase masks with fixed sinusoidal modulation, we can utilize wavefront matching algorithm to optimize temporal modulation phase while fixing the dispersion. This is equivalent to realizing the transformation through temporal modes. Temporal modulation implements arbitrary phase masks across temporal modes, and dispersion introduces relative time delay for inter-modal mixing (Fig. 4a). Figure 4b shows the optimization results (temporal modulation sequence and intermediate spectral distribution) with 4 transformation stages for input spectra with frequency separation $\delta = \sigma$. Spectral modes are obtained through Fourier transform of the temporal modes. We use a fixed second-order dispersion (group velocity dispersion) of the form $exp(-iDf^2)$ with $D = 0.03/\sigma^2$. The spectral HG_0 mode is well separated from HG_1 mode leading to FI surpassing direct detection (Fig. 5a). We see that resolution may be improved by a factor of ~ 25 using 6 stages, compared to direct detection.

Experimental implementation of this approach involves temporal phase modulation using arbitrary wave

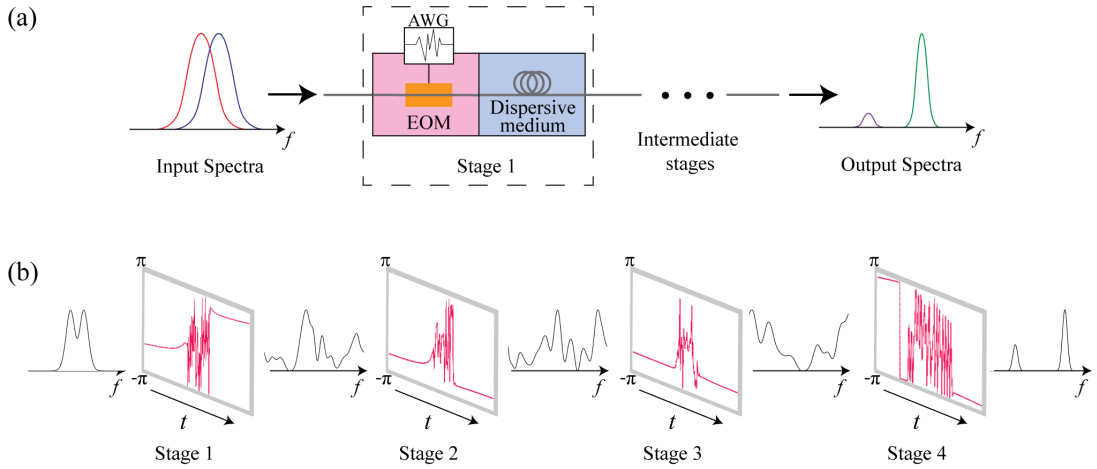

FIG. 4. (a) Schematic of spectro-temporal shaping with optimized temporal modulation and fixed dispersion. The fundamental and orthogonal higher-order HG modes of the input field are transformed into two well-separated Gaussian modes respectively. (b) Example results for a 4-stage spectral-temporal shaping, showing the applied temporal modulation (red) and output spectrum distribution (black) of each stage. Broad spectrum chosen here leads to sharp pulses that only require significant modulation phase change around the centre (t=0) of time axis. The fixed dispersion for all stages is $0.1/\sigma^2$ rad. The frequency separation between input spectral modes is $\delta = \sigma$. The dispersion phase is hidden for convenience.

generators. Its bandwidth directly determines the resolution of the temporal phase, which strongly influences the accuracy of the spectral-temporal transformation. Figure 5b shows the FI with varying modulation bandwidth and fixed group velocity dispersion $D = 0.03/\sigma^2$ using 6 transformation stages. Lowering the modulation bandwidth leads to larger error in implementing the optimized temporal phase. This gives rise to higher cross-talk and subsequently lower FI. A sufficiently high modulation bandwidth of $\sim 10\sigma$ is required to double the resolution compared to direct detection.

In addition, the amplitude of the group velocity dispersion directly determines the efficiency of inter-modal mixing in time domain. We show in Fig. 5c&d that a lowest-order dispersion (group velocity dispersion) of $\sim 0.015/\sigma^2$ is sufficient to introduce mixing among different temporal modes and achieve near-ideal FI. We observe an improvement in resolution by factor of 2 relative to direct detection.

IV. BINARY VS. FULL SPECTRAL-TEMPORAL TRANSFORMATION

Our discussion thus far has been limited to binary transformation strategy, which saturates the QCRB only in the small-δ regime (Fig. 1b). As δ increases, more information about the separation is contained in high-order HG modes and individual detection of each higher-order mode is needed to achieve higher FI. A full HG mode detection strategy, that transforms different input HG modes into a set of well-separated Gaussian modes at the output, can achieve the QFI for any frequency separation.

In Fig. 6a, we show the optimization result for the full

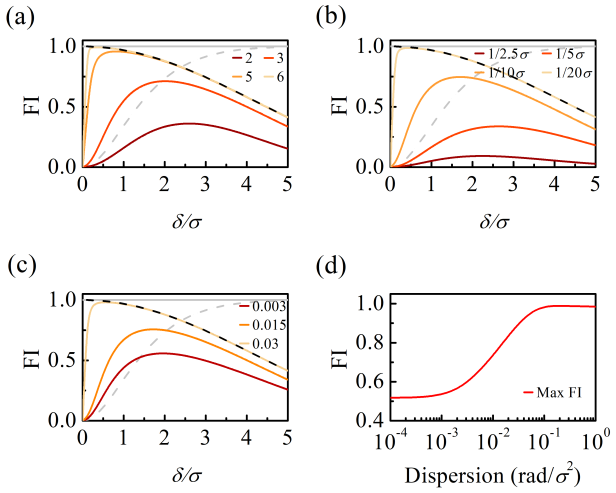

FIG. 5. Fisher information versus frequency separation optimized with (a) different numbers of transformation stages; (b) different temporal resolution of arbitrary wave modulation; and (c) total dispersion. Quantum Fisher information (solid grey), Fisher information of direct detection (dashed grey), and ideal binary transformation (dashed black) are also shown in (a-c). (d) Maximum achievable Fisher information with different total dispersion. Except specified, total dispersion is $0.03/\sigma^2$, bandwidth for arbitrary wave modulations is infinite, and number of transformation stages is 6.

HG mode detection implemented with optimized spectral phase masks and fixed sinusoidal modulation. We used 7 transformation stages and a modulation depth of 2.5π. We see that the achieved FI for full HG mode detection is significantly lower than the QFI. In comparison, the binary scheme implemented using identical parame-

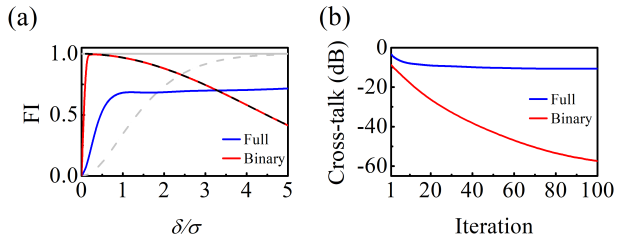

FIG. 6. (a) Fisher information versus frequency separation for full and binary HG mode transformation. Both optimizations are performed with 7 stages and modulation depth 2.5π. The QFI, direct detection Fisher information and ideal binary sorting Fisher information curves are replicated from Fig. 1; (b) Modal cross-talk vs. optimization iterations for full and binary transformation schemes.

ters performs significantly better than the full scheme for small frequency separation. For large frequency separation, direct detection outperforms both binary and full mode detection.

Optimized full HG mode transformation cannot achieve the highest FI in any frequency separation regime. This is because the complexity involved in the separation of all HG modes leads to excessive cross-talks with limited optimization resources (Fig. 6b). In contrast, binary transformation only requires the separation of HG_0 and HG_1 modes. Therefore, significantly lower cross-talk can be achieved with the same configuration. For this case, binary transformation has 50 dB lower cross-talk than full mode transformation (Fig. 6b), leading to a $10\times$ higher resolution. We infer that it is preferable to use binary transformation for frequency super-resolution due to its tolerance to cross-talk with fewer experimental resources.

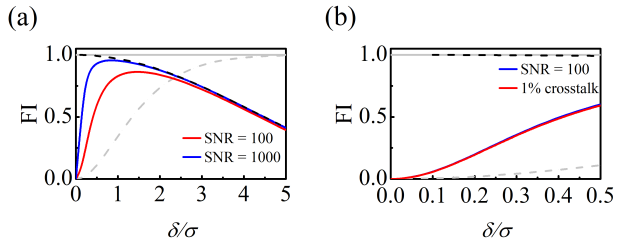

FIG. 7. (a) Fisher information against frequency separation for binary sorting with thermal noise of varied average photon number; (b) Comparison between Fisher information versus δ curves for binary sorting with noise (SNR = 100) and with 1% crosstalk. The QFI, direct detection Fisher information and ideal binary sorting Fisher information curves are replicated from Fig. 1.

V. NOISY DETECTION

In the preceding sections, we explore the impact of modal cross-talk on frequency resolution assuming noiseless photon detection. However, stray photons and dark counts may significantly influence the performance of these detection schemes [43, 53, 54] by introducing additional uncertainty in determining the power in the HG_1 mode for small δ. We factor in the effect of this noise as a weak thermal source emitting N_B photons on average within the detection window. The resultant probability of detecting a photon (using binary scheme) in the HG_1 mode is modified to,

$$P_1' = \left(1 - \frac{N_B}{N}\right)\left(1 - e^{\frac{\delta^2}{16\sigma^2}}\right) + \frac{N_B}{N} \tag{12}$$

For low noise level $N_B/N \ll 1$ and small frequency separation, the probability P_1' can be simplified to

$$P_1' = \left(1 - e^{\frac{\delta^2}{16\sigma^2}}\right) + \frac{1}{\mathrm{SNR}}. \tag{13}$$

where the signal-to-noise ratio (SNR) is given by N/N_B. Then the corresponding FI is expressed as

$$J_{b,B}(\delta) = \frac{N}{4\sigma^2}\left(\frac{\delta^2}{16\sigma^2}\right)\left(\frac{e^{-\frac{\delta^2}{8\sigma^2}}}{1 + \frac{1}{\mathrm{SNR}} - e^{-\frac{\delta^2}{16\sigma^2}}}\right). \tag{14}$$

In the small separation limit $\delta \to 0$, Eq.14 can be simplified to

$$J_{b,B}(\delta) = \frac{N}{4\sigma^2}\left(1 + 16\frac{\sigma^2}{\delta^2}\frac{1}{\mathrm{SNR}}\right)^{-1}. \tag{15}$$

Intuitively, lower noise level will lead to higher FI due to the more accurate measurement of optical power (Fig. 7a). It is also worth noting that noise has similar influence on FI with modal cross-talk, as both affect the measurement accuracy of HG_1 power. In Fig. 7b, FI with the same level of SNR and modal cross-talk is plotted. The FI for the two cases is nearly identical, indicating that any source of uncertainty in HG_1 modal power affects the FI equivalently.

VI. DISCUSSION

The two approaches discussed in the previous section are theoretically equivalent and connected by Fourier transform. However, the experimental choice of each approach depends critically on the bandwidth σ of the input field.

The optimized phase masks and sinusoidal temporal modulation can be readily realized with pulse shapers and electro-optic modulators driven with sinusoidal microwave signal. With high modulation efficiency and large bandwidth, we expect that electro-optic modulators would not constrain practical realization. On the other hand, the frequency resolution for pulse shapers is around 10 GHz. As shown in Fig. 3b, frequency super-resolution can be achieved if the frequency resolution of phase masks is smaller than $\sigma/1.5$. This determines that

the approach based on optimized phase masks only works for input field with bandwidths larger than 10s of GHz.

On the other hand, optimized temporal modulation requires electro-optic modulators driven with arbitrary waveform generators, whose bandwidth determines the temporal resolution. The group velocity delay can be simply realized with fiber spools and fiber Bragg gratings. As shown in Fig. 5b, temporal resolution smaller than $1/(10\sigma)$ is needed to demonstrate frequency super-resolution. Arbitrary waveform generators with bandwidth up to 80 GHz are commercially available. Therefore, it is possible to experimentally demonstrate frequency super-resolution with input field bandwidths smaller than 8 GHz. Depending on the input bandwidth (σ), we can select approach I /II for broad/narrow-band input frequency mode super-resolution, respectively.

Spectro-temporal shaping is not restricted to Gaussian modes and may be modified for input spectra with arbitrary mode shapes [55]. The modal basis for spectro-temporal shaping with alternate input shapes can be determined by using the input mode itself as the fundamental mode and constructing an orthonormal basis set [43]. A common example is the sinc-Bessel basis detection, which can achieve super-resolution for sinc-function input modes [31, 45].

We also note that the application of spectro-temporal shaping demonstrated here is not limited to two-mode problems. This treatment can be further extended for super-resolution of extended spectra and pulses [45]. It can also be applied to enhance the measurement resolution of time delay between two temporal pulses, based on the Fourier equivalence between time and frequency. This finds particularly important applications in optical measurement of distance, optical communications, oscilloscopes, and time-of-flight measurements.

VII. CONCLUSION

We have studied the approach to break the classical Rayleigh limit for frequency separation measurement. We show that the spectral-temporal shaping of input fields before detection can significantly increase FI and achieve frequency super-resolution. The two complementary methods based on the optimization of spectral phase masks and temporal modulation enable experimental implementation with feasible resource requirements. They also provide high flexibility to accomplish frequency super-resolution with different input bandwidths.

We further recognize that modal cross-talk due to imperfect transformation and detection noise have similar effect in the degradation of frequency resolution for practical applications. We find that binary transformation shows significantly better robustness than full mode transformation with limited resources, which is critical for the experimental implementation. In addition to new possibilities for spectroscopy, spectro-temporal shaping could also provide new insights for photonic processing such as arbitrary optical pulse generation and high-dimensional frequency-bin encoding of quantum information.

ACKNOWLEDGMENTS

This work was supported by Office of Naval Research (N00014-19-1-2190), and National Science Foundation (ECCS-1842559, CCF-1907918)

[1] S. F. Huelga, C. Macchiavello, T. Pellizzari, A. K. Ekert, M. B. Plenio, and J. I. Cirac, Improvement of frequency standards with quantum entanglement, Phys. Rev. Lett. **79**, 3865 (1997).
[2] T. Udem, R. Holzwarth, and T. W. Hänsch, Optical frequency metrology (2002).
[3] V. Giovannetti, S. Lloyd, and L. MacCone, Advances in quantum metrology (2011), arXiv:1102.2318.
[4] S. Mukamel, M. Freyberger, W. Schleich, M. Bellini, A. Zavatta, G. Leuchs, C. Silberhorn, R. W. Boyd, L. L. Sánchez-Soto, A. Stefanov, M. Barbieri, A. Paterova, L. Krivitsky, S. Shwartz, K. Tamasaku, K. Dorfman, F. Schlawin, V. Sandoghdar, M. Raymer, A. Marcus, O. Varnavski, T. Goodson, Z. Y. Zhou, B. S. Shi, S. Asban, M. Scully, G. Agarwal, T. Peng, A. V. Sokolov, Z. D. Zhang, M. S. Zubairy, I. A. Vartanyants, E. Del Valle, and F. Laussy, Roadmap on quantum light spectroscopy (2020).
[5] T. Ferreira da Silva, Photon-counting-based optical frequency metrology, Appl. Opt. **59**, 11232 (2020).
[6] E. C. Bullard, An atomic standard of frequency and time interval: Definition of the second of time, Nature **176**, 282 (1955).
[7] H. S. Margolis, Frequency metrology and clocks, J. Phys. B At. Mol. Opt. Phys. **42**, 154017 (2009).
[8] T. L. Nicholson, S. L. Campbell, R. B. Hutson, G. E. Marti, B. J. Bloom, R. L. McNally, W. Zhang, M. D. Barrett, M. S. Safronova, G. F. Strouse, W. L. Tew, and J. Ye, Systematic evaluation of an atomic clock at 2 10-18 total uncertainty, Nat. Commun. **6**, 1 (2015).
[9] I. Ushijima, M. Takamoto, M. Das, T. Ohkubo, and H. Katori, Cryogenic optical lattice clocks, Nat. Photonics **9**, 185 (2015).
[10] S. Albert, K. K. Albert, and M. Quack, High-Resolution Fourier Transform Infrared Spectroscopy, in *Handb. High-resolution Spectrosc.* (John Wiley Sons, Ltd, Chichester, UK, 2011).
[11] K. B. Beć, J. Grabska, and C. W. Huck, Biomolecular and bioanalytical applications of infrared spectroscopy – A review (2020).
[12] S. Mulleti, A. Singh, V. P. Brahmkhatri, K. Chandra, T. Raza, S. P. Mukherjee, C. S. Seelamantula, and

H. S. Atreya, Super-Resolved Nuclear Magnetic Resonance Spectroscopy, Sci. Rep. **7**, 1 (2017).
[13] M. A. Foster, R. Salem, D. F. Geraghty, A. C. Turner-Foster, M. Lipson, and A. L. Gaeta, Silicon-chip-based ultrafast optical oscilloscope, Nature **456**, 81 (2008).
[14] A. M. Weiner, Ultrafast optical pulse shaping: A tutorial review, Opt. Commun. **284**, 3669 (2011).
[15] H. Schnatz, B. Lipphardt, J. Helmcke, F. Riehle, and G. Zinner, *Phys. Rev. Lett.*, Tech. Rep. 1 (1996).
[16] T. Udem, J. Reichert, R. Holzwarth, and T. W. Hänsch, *Opt. Lett.*, Tech. Rep. 13 (1999).
[17] T. M. Fortier, A. Bartels, and S. A. Diddams, Octave-spanning Ti:sapphire laser with a repetition rate ¿1 GHz for optical frequency measurements and comparisons, Opt. Lett. **31**, 1011 (2006).
[18] N. Picqué and T. W. Hänsch, Frequency comb spectroscopy (2019).
[19] S. A. Diddams, K. Vahala, and T. Udem, Optical frequency combs: Coherently uniting the electromagnetic spectrum, Science (80-.). **369**, 10.1126/science.aay3676 (2020).
[20] T. Kobayashi, T. Sueta, Y. Cho, and Y. Matsuo, High-repetition-rate optical pulse generator using a Fabry-Perot electro-optic modulator, Appl. Phys. Lett. **21**, 341 (1972).
[21] M. Zhang, B. Buscaino, C. Wang, A. Shams-Ansari, C. Reimer, R. Zhu, J. M. Kahn, and M. Lončar, Broadband electro-optic frequency comb generation in a lithium niobate microring resonator (2019), arXiv:1809.08636.
[22] P. Del'Haye, A. Schliesser, O. Arcizet, T. Wilken, R. Holzwarth, and T. J. Kippenberg, Optical frequency comb generation from a monolithic microresonator, Nature **450**, 1214 (2007), arXiv:0708.0611.
[23] T. J. Kippenberg, R. Holzwarth, and S. A. Diddams, *Science (80-.)*., Tech. Rep. 6029 (2011).
[24] C. Wang, M. Zhang, M. Yu, R. Zhu, H. Hu, and M. Loncar, Monolithic lithium niobate photonic circuits for Kerr frequency comb generation and modulation, Nat. Commun. **10**, 1 (2019), arXiv:1809.08637.
[25] B. H. Kolner and M. Nazarathy, Temporal imaging with a time lens: erratum, Opt. Lett. **15**, 655 (1990).
[26] V. Torres-Company, J. Lancis, and P. Andrés, Spectral imaging system for scaling the power spectrum of optical waveforms, Opt. Lett. **32**, 2849 (2007).
[27] R. Salem, M. A. Foster, D. F. Geraghty, A. L. Gaeta, A. C. Turner, and M. Lipson, Time lens for ultrafast signal measurements based on four-wave mixing in silicon, in *Opt. InfoBase Conf. Pap.* (2008).
[28] Y. Okawachi, R. Salem, M. A. Foster, A. C. Turner-Foster, M. Lipson, and A. L. Gaeta, High-resolution spectroscopy using a frequency magnifier, Opt. Express **17**, 5691 (2009).
[29] B. H. Kolner, Space-Time Duality and the Theory of Temporal Imaging, IEEE J. Quantum Electron. **30**, 1951 (1994).
[30] Rayleigh, XXXI. Investigations in optics, with special reference to the spectroscope , London, Edinburgh, Dublin Philos. Mag. J. Sci. **8**, 261 (1879).
[31] M. Tsang, R. Nair, and X. M. Lu, Quantum theory of superresolution for two incoherent optical point sources, Phys. Rev. X **6**, 031033 (2016), arXiv:1602.04655.
[32] C. W. Helstrom, Quantum detection and estimation theory (1969).
[33] M. Paúr, B. Stoklasa, Z. Hradil, L. L. Sánchez-Soto, and J. Rehacek, Achieving the ultimate optical resolution, Optica **3**, 1144 (2016).
[34] M. Tsang, Quantum limit to subdiffraction incoherent optical imaging, Phys. Rev. A **99**, 10.1103/PhysRevA.99.012305 (2019), arXiv:1806.02781.
[35] M. R. Grace, Z. Dutton, A. Ashok, and S. Guha, Approaching quantum-limited imaging resolution without prior knowledge of the object location, J. Opt. Soc. Am. A **37**, 1288 (2020).
[36] T. Gefen, A. Rotem, and A. Retzker, Overcoming resolution limits with quantum sensing, Nat. Commun. **10**, 1 (2019), arXiv:1811.01762.
[37] J. M. Donohue, V. Ansari, J. Řeháček, Z. Hradil, B. Stoklasa, M. Paúr, L. L. Sánchez-Soto, and C. Silberhorn, Quantum-Limited Time-Frequency Estimation through Mode-Selective Photon Measurement, Phys. Rev. Lett. **121**, 10.1103/PhysRevLett.121.090501 (2018), arXiv:1805.02491.
[38] H. Cramér, *Math. Methods Stat.* (Princeton University Press, 2016).
[39] C. R. Rao, Information and the Accuracy Attainable in the Estimation of Statistical Parameters, in *Break. Stat.* (Springer, New York, NY, 1992) pp. 235–247.
[40] R. A. Fischer, On the mathematical foundations of theoretical statistics, Philos. Trans. R. Soc. London. Ser. A, Contain. Pap. a Math. or Phys. Character **222**, 309 (1922).
[41] C. W. Helstrom, Minimum mean-squared error of estimates in quantum statistics, Phys. Lett. A **25**, 101 (1967).
[42] S. L. Braunstein and C. M. Caves, *Phys. Rev. Lett.*, Tech. Rep. 22 (1994).
[43] Y. L. Len, C. Datta, M. Parniak, and K. Banaszek, Resolution limits of spatial mode demultiplexing with noisy detection, Int. J. Quantum Inf. **18**, 1941015 (2020).
[44] B. Brecht, D. V. Reddy, C. Silberhorn, and M. G. Raymer, Photon temporal modes: A complete framework for quantum information science, Phys. Rev. X **5**, 10.1103/PhysRevX.5.041017 (2015), arXiv:1504.06251.
[45] Z. Dutton, R. Kerviche, A. Ashok, and S. Guha, Attaining the quantum limit of superresolution in imaging an object's length via predetection spatial-mode sorting, Phys. Rev. A **99**, 33847 (2019), arXiv:1801.06602.
[46] J. M. Lukens and P. Lougovski, Frequency-encoded photonic qubits for scalable quantum information processing, Optica **4**, 8 (2017), arXiv:1612.03131.
[47] H. H. Lu, J. M. Lukens, N. A. Peters, O. D. Odele, D. E. Leaird, A. M. Weiner, and P. Lougovski, Electro-Optic Frequency Beam Splitters and Tritters for High-Fidelity Photonic Quantum Information Processing, Phys. Rev. Lett. **120**, 30502 (2018), arXiv:1712.03992.
[48] J.-F. Morizur, L. Nicholls, P. Jian, S. Armstrong, N. Treps, B. Hage, M. Hsu, W. Bowen, J. Janousek, and H.-A. Bachor, Programmable unitary spatial mode manipulation, J. Opt. Soc. Am. A **27**, 2524 (2010), arXiv:1005.3366.
[49] N. K. Fontaine, R. Ryf, H. Chen, D. T. Neilson, K. Kim, and J. Carpenter, Laguerre-Gaussian mode sorter, Nat. Commun. **10**, 1 (2019), arXiv:1803.04126.
[50] M. Mazur, N. K. Fontaine, R. Ryf, D. T. Neilson, H. Chen, G. Raybon, A. Adamiecki, S. Corteselli, and J. Schröder, Optical Arbitrary Waveform Generator Based on Time-Domain Multiplane Light Conversion, in

Opt. Fiber Commun. Conf. 2019, 1 (OSA, Washington, D.C., 2019) p. M1B.3.

[51] Y. Sakamaki, T. Saida, T. Hashimoto, and H. Takahashi, New optical waveguide design based on wavefront matching method, J. Light. Technol. **25**, 3511 (2007).

[52] M. Gessner, C. Fabre, and N. Treps, *Phys. Rev. Lett.*, Tech. Rep. 10 (2020) arXiv:2004.07228.

[53] C. Lupo, Subwavelength quantum imaging with noisy detectors, Phys. Rev. A **101**, 22323 (2020), arXiv:1911.10012.

[54] C. Oh, S. Zhou, Y. Wong, and L. Jiang, *arXiv*, Tech. Rep. (2020) arXiv:2008.11339.

[55] R. Kerviche, S. Guha, and A. Ashok, Fundamental limit of resolving two point sources limited by an arbitrary point spread function, in *IEEE Int. Symp. Inf. Theory - Proc.* (Institute of Electrical and Electronics Engineers Inc., 2017) pp. 441–445, arXiv:1701.04913.